Check for updates

ADVANCED OPTICAL MATERIALS
www.advopticalmat.de

Liquid-Phase Transfer of Organic–Inorganic Halide Perovskite Films for TEM Investigation and Planar Heterojunction Fabrication

Shuai Guo, Xiangzhao Zhang, Mingwei Hao, Tianwei Duan, Weizhen Wang, Zhimin Li, Guiwu Liu, Songhua Cai, and Yuanyuan Zhou**

Organic–inorganic halide perovskites (OIHPs) show high promise in optical and electronic applications such as solar cells, light-emitting diodes, and nonlinear optics. However, the fundamental knowledge of the atomic-scale microstructures in OIHP thin films is limited due to the challenge in characterizing them using transmission electron microscopy (TEM). Here a solution-phase "release-and-transfer" method is demonstrated, which entails the lifting of OIHP films from their original substrates while maintaining the film integrity, followed by a sequential transfer onto a TEM grid. The freestanding nature of the OIHP films with a nanoscale thickness, prepared as such, allows a direct TEM observation in the plan view, complementing those typical cross-sectional views enabled by focus-ion-beam specimen fabrication. Using low-dose scanning TEM, the atomic-scale microstructure of transferred OIHP films is confirmed to be generally maintained, while the microstrain existing in original films is largely relaxed. This "release-and-transfer" method is generic to both standard 3D and low-dimensional OIHPs. Based on a simple layer-by-layer transfer, the fabrication of a 2D–3D planar heterojunction with a good interfacial contact and optoelectronic properties is achieved. This unique methodology offers new opportunities to accelerate the fundamental and practical developments of OIHP materials and devices.

1. Introduction

As a new class of unconventional semiconductors, organic–inorganic halide perovskites (OIHPs) have shown outstanding optical and electronic properties, such as tunable bandgaps and carrier mobilities, high photoluminescence (PL) quantum yield, and high light-absorption coefficients.[1–3] The standard chemical formula of OIHPs is ABX_3, where A is a monovalent organic or metal cation, B is a divalent metal cation, and X is Cl, Br, or I. The crystal structure and properties are easily tailorable by manipulating the ions at the A, B, and X sites of OIHPs, unleashing numerous possibilities for device development.[4–6] This has led to a rapid improvement in the power conversion efficiencies (PCEs) of perovskite solar cells (PSCs), attaining certified 25.8% in only about one decade.[7] Also, owing to the relatively soft nature, OIHPs demonstrate their high suitability for flexible and integrable application scenarios.[8–10] Nevertheless, the materials and device engineering of OIHPs reported so far have been mostly limited to the nanometer to micrometer scale. In this context, there is an urgent need for tailoring OIHP thin films at the atomic scale, which can lead to the next leap in perovskite technologies. The most prominent step toward that goal is to acquire the atomic-scale microstructural details in OIHP thin films.

Transmission electron microscopy (TEM) is one of the most powerful tools for microstructural characterization and

S. Guo, T. Duan, W. Wang, Z. Li, S. Cai
Department of Applied Physics
The Hong Kong Polytechnic University
Hong Kong SAR 999077, China
E-mail: songhua.cai@polyu.edu.hk

X. Zhang, M. Hao, Y. Zhou
Department of Physics
Hong Kong Baptist University
Hong Kong SAR 999077, China
E-mail: yyzhou@ust.hk

X. Zhang, G. Liu
School of Materials Science and Engineering
Jiangsu University
Xuefu Road, Zhenjiang, Jiangsu 212013, China

Y. Zhou
Department of Chemical and Biological Engineering
The Hong Kong University of Science and Technology
Clear Water Bay, Hong Kong SAR 999077, China

The ORCID identification number(s) for the author(s) of this article can be found under https://doi.org/10.1002/adom.202301255

© 2023 The Authors. Advanced Optical Materials published by Wiley-VCH GmbH. This is an open access article under the terms of the Creative Commons Attribution-NonCommercial License, which permits use, distribution and reproduction in any medium, provided the original work is properly cited and is not used for commercial purposes.

DOI: 10.1002/adom.202301255

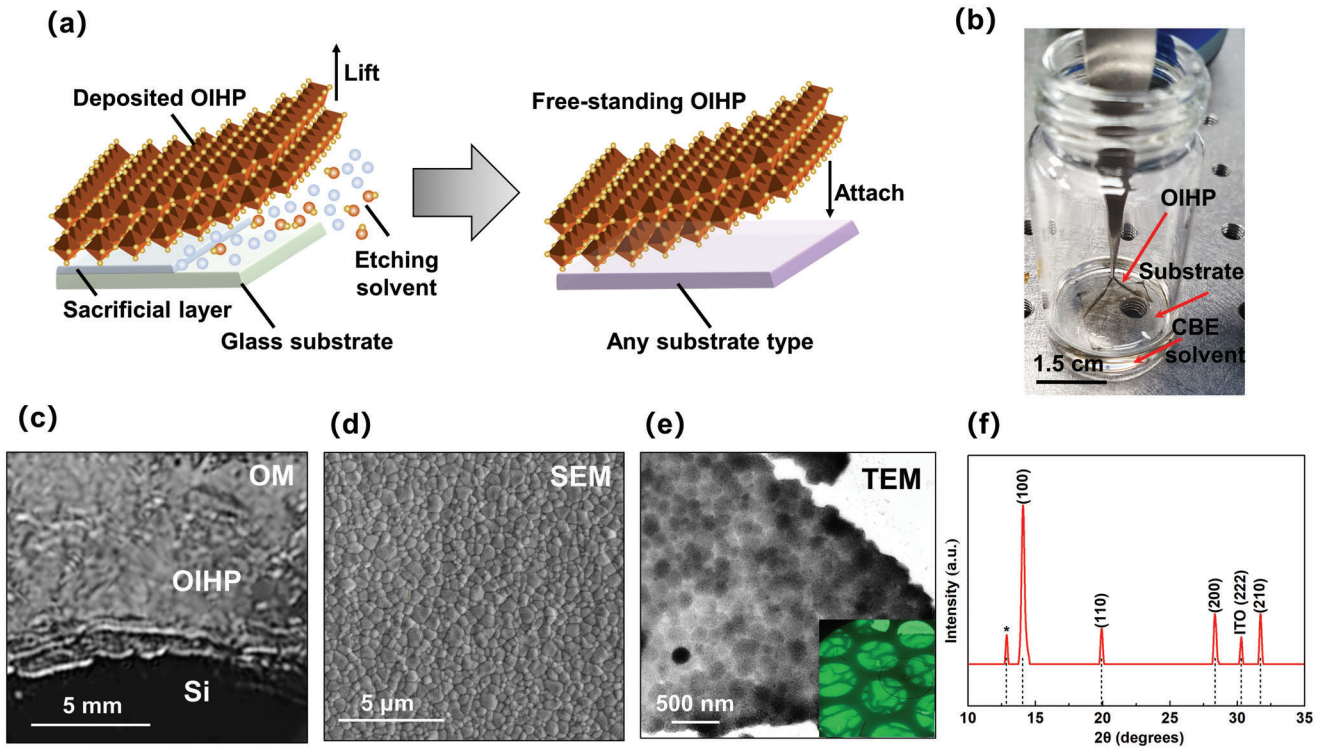

Figure 1. RAT method for OIHP films ($FA_{0.9}Cs_{0.07}MA_{0.03}Pb(I_{0.92}Br_{0.08})_3$): a) Schematic illustration showing the solution-phase RAT process of an OIHP film with a PS sacrificial layer. The sacrificial layer is dissolved in CBE to release the top perovskite. New heterostructures and interfaces are formed when the freestanding film is transferred onto another chosen substrate. b) Photograph of an OIHP film being released from the substrate in CBE using a tweezer. c) Optical microscopy (OM) image and d) SEM image of the OIHP film transferred onto a silicon substrate. e) TEM image of the OIHP film transferred onto a TEM copper gird. Inset is the OM image of the TEM fluorescent screen showing copper gird covered by OIHP film. f) XRD pattern of the OIHP film after the RAT process.

local-composition determination.[11] The unique high spatial resolution makes TEM recognized as the best method to characterize material structures at the subatomic scale.[12] The recent use of low-dose scanning TEM (STEM), in conjunction with the focused ion beam (FIB) based specimen nanofabrication, has unlocked rich atomic-scale details in the OIHP films. However, the involvement of FIB fabrication increases the instrumental requirement, experimental complexity, as well as significant investment of time and effort. Also, FIBed specimens only provide cross-sectional views of OIHP films and devices, while plan views are still necessary in order to visualize the complete atomic landscape in OIHPs. In this regard, we report a solution-phase "release-and-transfer (RAT)" method that enables us to release the OIHP thin film from its original substrate and then simply place it on the TEM grid for later characterization. Note that although vapor or solution deposition of OIHPs directly onto the TEM grids can be an alternative method to investigate OIHP films in plan views,[13–15] the thickness, uniformity, and morphology of the film specimen are hardly controllable due to the wetting issues of typical TEM grids (with supporting carbon films). Importantly, the impact of the RAT method is beyond meeting the need for TEM investigation. Since RAT allows for the transfer of perovskite films with varied compositions and thicknesses while maintaining the microstructural integrity and properties, it paves a facile way to fabricate planar heterojunctions of different OIHPs via a simple layer-by-layer stacking. A 2D–3D OIHP heterojunction is fabricated as a proof-of-concept demonstration.

2. Results and Discussion

2.1. Liquid-Phase RAT of OIHP Films

Formamidinium-cesium (FA-Cs) OIHPs, which can exhibit both high PCEs and stability in perovskite solar cells, are used to demonstrate the liquid-phase RAT and to examine its potential influence on the film microstructure and optoelectronic properties.[16–19] OIHP films with two 3D perovskites, $FA_{0.8}Cs_{0.2}PbI_3$ and $FA_{0.9}Cs_{0.07}MA_{0.03}Pb(I_{0.92}Br_{0.08})_3$, and one 2D perovskite, $(PEA)_2MAPb_2I_7$ have been successfully transferred, validating the generality of this method. Preparation details for these films have been included in the Experimental Section.

Figure 1a schematically illustrates the solution-phase RAT method for OIHPs. Herein we incorporated a polystyrene (PS) interlayer between the OIHP films and substrate, and the PS serves as a sacrificial layer. Typically, a smooth polycrystalline OIHP thin film was deposited on a PS-coated glass substrate. Then, the OIHP film was immersed in a chlorobenzene (CBE) solvent, following which the PS sacrificial layer was gradually dissolved. As a result, the OIHP film becomes freestanding, which can be easily lifted out and transferred onto another chosen substrate. This approach allows the successful transfer of the entire

© 2023 The Authors. Advanced Optical Materials published by Wiley-VCH GmbH

21951071, 2024, 8, Downloaded from https://onlinelibrary.wiley.com/doi/10.1002/adom.202301255 by Hong Kong Poly University, Wiley Online Library on [17/06/2024]. See the Terms and Conditions (https://onlinelibrary.wiley.com/terms-and-conditions) on Wiley Online Library for rules of use; OA articles are governed by the applicable Creative Commons License

perovskite films of a large area. Figure 1b is a photograph showing a released OIHP film of 2.25 cm^2 in the CBE solvent. The released OIHPs film can easily be transferred using the tweezer onto a silicon wafer and glass as shown in Figure 1c; and Figure S1 (Supporting Information). Top-view scanning electron microscopy images (Figure 1d; and Figure S2, Supporting Information) confirm the retention of the compact polycrystalline film morphology after the RAT process. More importantly, by transferring the released OIHP film onto a regular TEM copper grid (covered by a holey carbon supporting film (Figure 1e), the morphology and atomic-scale microstructure of OIHPs become immediately characterizable using TEM imaging and diffraction methods, enabling in-depth investigations. To enable the high-quality and high-resolution TEM observation of the transferred OIHP films' microstructures, the thickness of the OIHP films (Figure S3, Supporting Information) will be tailored to ≈50 nm in the spin-coating procedure. Moreover, the OIHP films' thicknesses can be adjusted for specific requirements. We also obtained the X-ray diffraction (XRD) pattern of the transferred OIHP film (on an ITO glass substrate), showing good phase purity (Figure 1f). Maintaining the integrity of the crystalline microstructure in OIHPs is paramount in achieving good optoelectronic properties.[20,21] The XRD results also indicate that the transferred OIHP films still retain the original long-range structural ordering without notable damage from the transfer process. There is a diffraction peak at $2\theta = 12.8°$ near (100) which can be attributed to PbI_2.[22] The existence of PbI_2 impurities in the transferred OIHP film can be attributed to either the residual PbI_2 from OIHP synthesis (Figure S4b, Supporting Information) or further exposure to the ambient moisture during processing and characterization. In fact, it is not uncommon to observe a slight excess of PbI_2 in high efficient perovskite solar cells fabricated by different approaches.[23–25] While the presence of PbI_2 impurities is not necessarily detrimental to device performance, we expect a minimization of air exposure in the transfer process can lead to better control over the PbI_2 formation.[26,27] We also measured the state-state PL spectrum of the transferred OIHP which exhibits an emission centered at 792 nm (Figure S4a, Supporting Information), similar to the case of the original film.[28]

2.2. Atomic-Scale Characterizations of OIHP Films

While the microstructure integrity and film quality of OIHPs by RAT have been validated, there is a potential alteration in microstructures at the atomic scale, coupled with the strain relaxation, which generates impacts on the film properties. Thus, atomic-scale insights into OIHPs' microstructures before and after RAT are essential to uncover such structure and property variations. Note here that only film samples with a thickness of less than 100 nm can be used to acquire the atomic information of OIHPs under TEM. In a recent study, we reported a simple, modified low-dose STEM method in conjunction with a special post-protection to OIHPs by conductive layers, which allows a direct, reliable observation of perovskite microstructures.[27] This development allowed us to coat 10 nm C60 film onto the top surface of the OIHPs film transferred onto the copper grid before STEM observation in order to mitigate electron-beam damage. The grain morphology of the as-transferred OIHP film is observed by low-magnification high angle annular dark field (HAADF)-STEM as shown in **Figure 2**a. The grain sizes of this OIHP film are around several hundred nanometers, consistent with TEM result shown in Figure 1e. The signal-to-noise ratio (SNR) of conventional STEM imaging with annular detectors will deteriorate with decreased electron dose for high-resolution STEM characterizations of OIHPs, resulting in reduced image quality and hiding the real structural information, even though electron beam damage in beam-sensitive materials can be effectively prevented under low-dose imaging conditions.[12] Recently, a newly-developed integrated differential phase contrast (iDPC) STEM approach has been utilized in the atomic-scale characterizations of beam-sensitive materials, such as zeolites.[29,30] This unique iDPC-STEM method works by detecting the deflection of incident electrons using a segmented detector instead of an annular detector, demonstrating great potential in obtaining high SNR images even at extremely low electron doses.[31] In this work, we used both HAADF-STEM and iDPC-STEM to investigate the lattice structure of as-transferred and pristine $FA_{0.8}Cs_{0.2}PbI_3$ films from different scales. The beam current of the electron probe used for STEM imaging is decreased to 2 pA to minimize the potential damage to the perovskite framework, and the zone-axis of OIHP grain was finely tuned before image acquisition to ensure the data validation. The high-resolution HAADF-STEM image and corresponding fast Fourier transform (FFT) pattern shown in Figure 2b indicate that the OIHP grain is projected along the [100] direction. From the higher magnified HAADF-STEM image (Figure 2c), the lattice spacing of (010) face is measured as 6.22 Å, which corresponds to the cubic phase of OIHP. Besides, the Pb columns in Figure 2c exhibit the highest contrast compared to the FA/Cs and I columns (Figure S5, Supporting Information), consistent with the Z-contrast of HAADF-STEM. As iDPC-STEM can maintain a higher SNR for low-dose imaging compared with HAADF-STEM, the detailed atomic structure of the as-transferred OIHP is unveiled by the high-resolution iDPC-STEM image shown in Figure 2d, with both FA/Cs, Pb and I atomic columns clearly revealed. The observed lattice structure also accurately fits the structure model of cubic $FACsPbI_3$ (Figure 2d).[32]

OIHPs synthesized via solution-based processes at low temperatures are commonly polycrystalline,[33] resulting in inherent inhomogeneities in perovskite films. This will easily lead to localized intragrain lattice mismatch and nonuniform strain, thus resulting in divergent electronic properties even within the same grain.[34,35] To investigate the intragrain strain conditions in solution-synthesized OIHPs films before and after RAT, geometric phase analysis (GPA) strain mapping was employed to extract the strain distribution from high-resolution HAADF-STEM images. Although the released freestanding OIHP film can be transferred onto TEM grid for direct STEM observation, the preparation of TEM specimen from the as-synthesized OIHP film with its original substrate will be more complicated. Therefore, we first prepared the cross-sectional specimens of both the pristine and as-transferred OIHP films through FIB fabrication to maintain the boundary conditions of different samples and the sample preparation consistency. The HAADF-STEM images of the pristine (Figure 2e) and as-transferred OIHP film (Figure 2h) were then taken along the [001] projection direction (Figure S6, Supporting Information) for intragrain strain analysis. Further

© 2023 The Authors. Advanced Optical Materials published by Wiley-VCH GmbH

21951071, 2024, 8, Downloaded from https://onlinelibrary.wiley.com/doi/10.1002/adom.202301255 by Hong Kong Poly University, Wiley Online Library on [17/06/2024]. See the Terms and Conditions (https://onlinelibrary.wiley.com/terms-and-conditions) on Wiley Online Library for rules of use; OA articles are governed by the applicable Creative Commons License

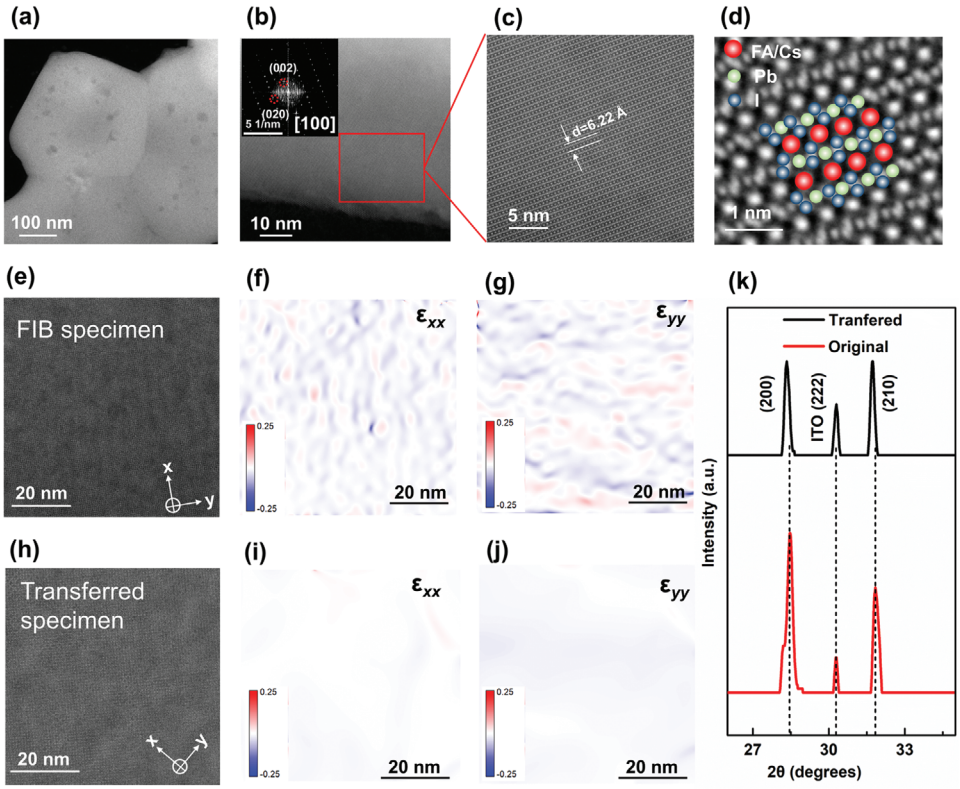

Figure 2. Atomic structures and strain conditions of OIPHs ($FA_{0.8}Cs_{0.2}PbI_3$). a) HAADF-STEM image of OIHPs at low magnification. b) High-resolution HAADF-STEM image of a $FA_{0.8}Cs_{0.2}PbI_3$ grain observed from [100] projection direction. The inset is the corresponding FFT pattern. c) High-resolution HAADF-STEM image taken from the region marked by the red square in (b). d) Atomic-resolution iDPC-STEM image shows the fine atomic structure of the OIHPs. e,h) High-resolution HAADF-STEM images taken from [001] projection direction of pristine (cross-section specimen of OIHP film deposited on ETL prepared by FIB) and as-transferred (plan-view specimen prepared by transferring the OIHP film onto TEM copper grid) OIHPs, respectively. f,g,i,j) Corresponding intragrain strain ϵ_{xx} and ϵ_{yy} distributions of (e) and (h) generated by GPA analysis. k) XRD spectra of OIHPs before and after transfer. Only a small range of 2θ is presented to show the shift of diffraction peak positions.

information regarding GPA is available in our previously published article.[27] The strain existing in perovskites typically originates from two distinct sources: local lattice strain and externally induced strain.[36] The local lattice strain is an inherent material property, which will not be discussed in detail here. The focus of this study is on externally induced strain, which can be further divided into two types: thermal expansion and lattice mismatch between the perovskite and substrate. Original OIHPs are annealed at 90 °C for 30 min after being spin-coated onto ITO-coated glass. In comparison to the thermal expansion coefficient (0.37 to 1×10^{-5} K^{-1}) of ITO-coated glass, perovskite films exhibit a higher volumetric thermal expansion coefficient (α_v) for cubic perovskites, ranging from 9.9 to 25.2×10^{-5} K^{-1}.[37,38] Due to the substantial difference in thermal expansion coefficients between the substrate and perovskite film, strain (σ) occurs when the temperature decreases. The temperature-induced strain ($\sigma_{\Delta T}$) can be described by the following equation[31]

$$\sigma_{\Delta T} = \frac{E_P}{1 - \nu_P} \left(\alpha_S - \alpha_P\right) \Delta T \quad (1)$$

where ν_P is the Poisson's ratio of perovskite, ΔT represents the temperature change, E_P signifies the modulus of perovskite, and α_P and α_S denote the thermal expansion coefficients of perovskite and substrate, respectively. This equation illustrates that strain depends on the thermal expansion coefficients and temperatures of the two materials. The higher thermal expansion coefficient of OIHPs results in compressive stress after cooling. Compressive or tensile stresses caused by lattice mismatch depend entirely on the difference in crystal plane spacing $d(hkl)$ between the substrate and perovskite.[31] Consequently, the random distribution of compressive and tensile intragrain strain in both the x and y directions for the pristine OIHPs specimen can be observed from the strain mapping results generated by GPA analysis shown in Figure 2f,g. In comparison, the intragrain nonuniform strain of as-transferred OIHP film released from PS surface is virtually negligible, indicating that this transfer approach enables the relaxation of intragrain strain in OIHP grains formed by synthesis conditions. In addition, a similar phenomenon is found in the freestanding OIHP film transferred onto the TEM grid. From the GPA analysis of a high-resolution HAADF-STEM image taken from a perovskite grain observed along [100] projection direction, the intragrain strain distribution exhibits little divergence in both directions (Figure S7, Supporting Information). To investigate the factors that influence strain relaxation, we carefully examined the OIHP films spin-coated onto PS substrate before (Figure S8a, Supporting Information) and after the transfer processes (Figure S8d, Supporting Information) (both

© 2023 The Authors. Advanced Optical Materials published by Wiley-VCH GmbH

21951071, 2024, 8, Downloaded from https://onlinelibrary.wiley.com/doi/10.1002/adom.202301255 by Hong Kong Poly University, Wiley Online Library on [17/06/2024]. See the Terms and Conditions (https://onlinelibrary.wiley.com/terms-and-conditions) on Wiley Online Library for rules of use; OA articles are governed by the applicable Creative Commons License

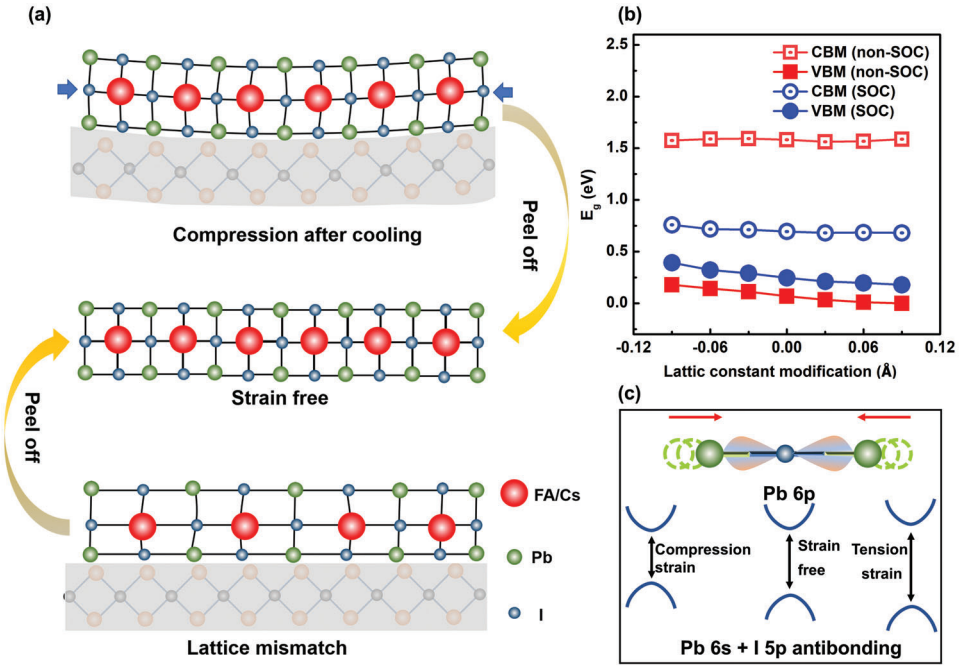

Figure 3. a) Illustration of the strain relaxation process of $FAPbI_3$ perovskite film. Upon peeling off the film from the substrate, the compressive strain induced by different coefficients of thermal expansion is effectively mitigated, while the microstrain resulting from lattice mismatch is simultaneously alleviated. b) The correlation between the variation of the lattice constants and the bandgap. Specifically, the DFT calculation solely takes into account the impact of strain-induced lattice constant variation, while other factors are not incorporated into our model. c) A schematic illustration is presented to depict the evolution of the bandgap in $FAPbI_3$ perovskite under varying degrees of strain, from compression to tension.

prepared by similar FIB processing) from the cross-sectional perspective. As seen in Figures S8b,c (Supporting Information), the intragrain strain of the OIHP film prepared by spin-coating on the PS substrate is more remarkable than that of prepared on ITO substrate (Figure 2e), as well as the transferred films (Figure 2h). This difference can be attributed to the higher coefficient of thermal expansion of PS (8×10^{-5} K^{-1}) than ITO or OIHP film, which will result in strain concentration in OIHP films during annealing and cooling. For transferred OIHPs films, compared with the direct plane-view observation of as-transferred film in Figure 2i,j; and Figure S8e,f (Supporting Information) demonstrate a bit larger intragrain strain after FIB preparation of the as-transferred film's cross-sectional specimen, indicating the potential influence of FIB processing induced thermal effect on the strain states of the films. It is worth noting that while the FIB processing may lead to additional strain within the film, the transferred film still exhibits a relaxed intragrain strain compared to the film deposited on either the ITO or PS substrates, as shown in Figure 2f,g; and Figure S8a–c (Supporting Information). This suggests the transfer approach can effectively reduce the intragrain strain resulting from the differences in thermal expansion coefficients and lattice mismatch between OIHPs films and substrates. While high-resolution STEM can provide localized lattice information, XRD is capable of getting extensive crystallographic information. The congruent peak positions between the pristine and as-transferred OIHP films indicate that the transfer processes do not alter the lattice structure of the OIHPs (Figure 2k). Interestingly, a detailed comparison of the pristine and the as-transferred film implies a slight difference with a small shift of diffraction peaks to lower 2θ for the transferred film from XRD result, representing a lattice expansion after the transfer process. This variation in lattice constant after film transfer may be associated with the lattice strain relaxation observed by high-resolution STEM,[39] which may affect the physical property of the as-transferred OIHPs.[29]

2.3. DFT Analysis of Strain and Bandgap

As previously discussed, the primary source of strain in the perovskite film is attributable to the discrepancy between the coefficients of thermal expansion and the lattice mismatch between the perovskite and substrate. This strain can be entirely alleviated through a RAT process (**Figure 3**a), resulting in a lattice expansion of the film once it has been transferred (Figure 2k). Figure 3b shows the calculated bandgaps of $FAPbI_3$ under triaxial compression or tension with/without the spin–orbital coupling (SOC) effect. Notably, the inclusion of SOC has a significant impact on the bandgap of $FAPbI_3$, regardless of whether triaxial compression or tension is applied. This is mainly attributed to the splitting of the Pb *6p* states. Both the non-SOC and SOC bandgaps of $FAPbI_3$ gradually increase as the lattice parameters increase, due to the strain relaxation behavior that occurs when the organic–inorganic hybrid perovskite (OIHP) is peeled off from the substrate. Furthermore, during this process, the conduction band minimum (CBM) remains almost unchanged, while the valence band maximum (VBM) gradually decreases. It is well-known that the CBM of the $FAPbI_3$ perovskite is primarily governed by the nonbonding Pb *6p* orbital, whereas the VBM consists mainly of I *5p* and Pb *6s* antibonding states. In Figure 3c, it can be observed

© 2023 The Authors. Advanced Optical Materials published by Wiley-VCH GmbH

21951071, 2024, 8, Downloaded from https://onlinelibrary.wiley.com/doi/10.1002/adom.202301255 by Hong Kong Poly University, Wiley Online Library on [17/06/2024]. See the Terms and Conditions (https://onlinelibrary.wiley.com/terms-and-conditions) on Wiley Online Library for rules of use; OA articles are governed by the applicable Creative Commons License

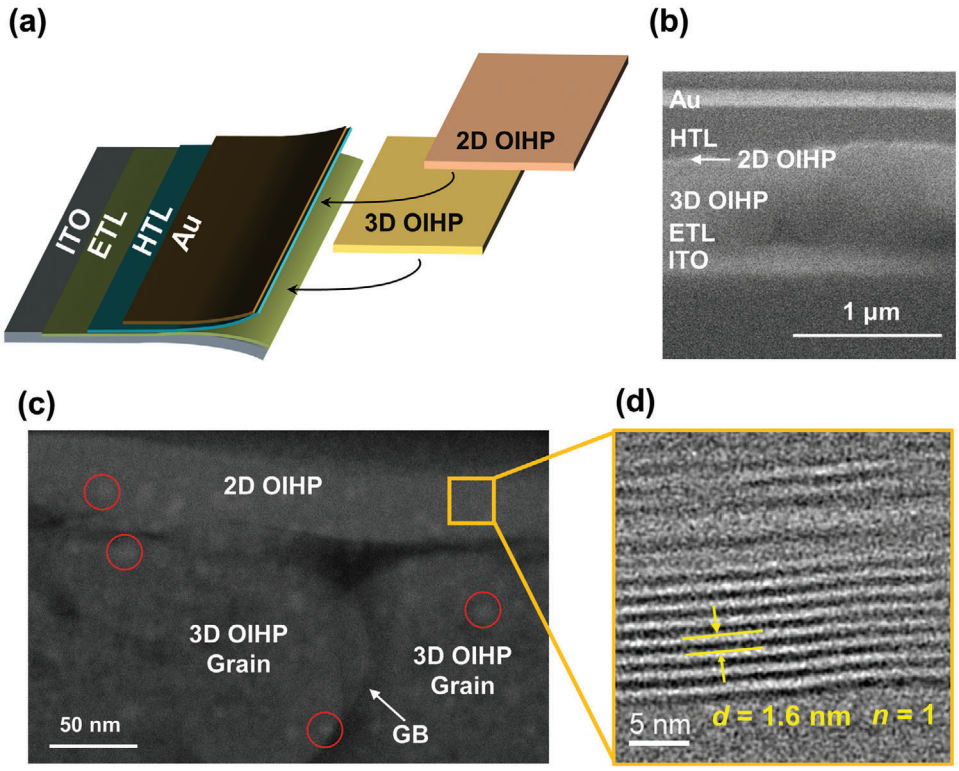

Figure 4. Planar perovskite heterojunctions solar cell fabrication through RAT processes. a) The solar cell architecture is depicted, wherein the cells can be constructed in two types, both utilizing freestanding 3D OIHP ($FA_{0.9}Cs_{0.07}MA_{0.03}Pb(I_{0.92}Br_{0.08})_3$) and 2D OIHP ($(PEA)_2MAPb_2I_7$) films—comprising either a purely 3D OIHP film or a 2D–3D heterojunction stacked by 2D and 3D OIHP films. b) Low-magnification SEM image of FIB-prepared 2D–3D heterojunction solar cell cross-section specimen, providing insights into the morphology of the heterojunction and its constituent layers. c) HAADF-STEM image of FIB-prepared 2D–3D heterojunction solar cell cross-section specimen is provided, allowing for a more detailed visualization and analysis of the heterojunction interface. d) A magnified HAADF-STEM image taken from yellow squared region in (c) is shown, offering a glimpse into the nanoscale features of 2D OIHP film in the heterojunctions.

that the $[PbI_6]^{4-}$ octahedral structure undergoes an expansion after peeling off, resulting in an elongation of the Pb—I—Pb bond length, which, in turn, leads to a reduction in electron cloud overlap between Pb *6s* and I *5p* orbitals. Consequently, the energy of the VBM decreases due to the reduced interaction between the two orbitals, while the CBM remains unaffected, given the nonbonding nature of the Pb *6p* orbital. Although strain relaxation may slightly increase the bandgap of the perovskite, moving toward a strain-free state may ultimately help enhance the stability and efficiency of solar cells.[40] Especially, the formation energy of the halide vacancies in OIHPs decreases with increasing tensile strain.[39,41] Furthermore, the intragrain strain may affect the carrier dynamics of the solar cells by bending the energy band of the OIHP absorber.[42,43]

2.4. Planar Heterojunction Fabrication by As-Transferred OIHPs Films

To demonstrate the practical application of the RAT method in perovskite photovoltaic devices, we transferred the OIHP films onto ITO glass substrates with spin-coated ETL layers and subsequently fabricated PSC devices. In addition to the 3D OIHPs films, we further synthesized and transferred the $(PEA)_2MAPb_2I_7$ 2D perovskite film through a similar method (Figure S10, Supporting Information) for the construction of different structured devices. Two distinct typed PSC devices were fabricated as shown in **Figure 4**a, one comprised a 2D–3D OIHP planar perovskite heterojunctions (Figure S11, Supporting Information) prepared through the van der Waals stacking of the freestanding 2D and 3D OIHP films, while the other comprised a purely 3D OIHP film (Figure S12, Supporting Information). To characterize the microstructures of as-fabricated PSC devices prepared through OIHP film transfer, the cross-section specimens were prepared by FIB to exhibit the layered and interfacial structures in PSCs. SEM image (Figure 4b) of the 2D–3D PSC cross-sectional specimen demonstrates that the transferred and van der Waals stacked 2D and 3D OIHP layers are in close contact. The 3D PSC cross-section specimen (Figure S13, Supporting Information) also shows a typical solar cell structure with the OIHP film maintaining its integrity. Figures S14 and S15 (Supporting Information) present the *J–V* curves of the 2D–3D PSC and 3D PSC devices measured from reverse scanning under simulated AM 1.5G one-sun illumination, confirming the effectiveness of PSCs devices fabricated from as-transferred OIHPs films. Besides, the interface between the 2D and 3D OIHP layers is observed by HAADF-STEM (Figure 4c), exhibiting a continuous 2D perovskite layer on the 3D top surface. It is worth

© 2023 The Authors. Advanced Optical Materials published by Wiley-VCH GmbH

21951071, 2024, 8, Downloaded from https://onlinelibrary.wiley.com/doi/10.1002/adom.202301255 by Hong Kong Poly University, Wiley Online Library on [17/06/2024]. See the Terms and Conditions (https://onlinelibrary.wiley.com/terms-and-conditions) on Wiley Online Library for rules of use; OA articles are governed by the applicable Creative Commons License

noting that the white bubble-like regions marked by red circles in Figure 4c represent the potential degradation induced by electron-beam irradiation or sample preparation/operation. Such degradation is difficult to avoid especially for OIHPs with higher organic-cation content, and similar phenomena can be observed even at a very low electron beam dose and temperature.[12] The layered structure of 2D OIHP is visible from a high-resolution HAADF-STEM image (Figure 4d) and, with the distance between each layer measured as 1.6 nm, corresponding to $n = 1$ 2D perovskite. The 3D perovskite grain in Figure 4c is also examined by high-resolution iDPC-STEM at atomic-scale along the [100] and [001] projection directions (Figure S16, Supporting Information), indicating the well-maintained perovskite structure. These results confirm that the RAT processes are applicable for stacking perovskite films while maintaining their structural integrity and physical properties for device applications. Recent advances in TEM characterization of OIHPs have demonstrated the possibility of producing unprecedented local structure/phase information as well as the potential relationship with OIHPs' properties and devices' performances.[14,15,44,45] OIHPs can be easily processed into thin films at low temperatures using various methods, and their compositions and crystal structure are extremely complicated, which leads to the incomprehension of the relationship between OIHPs' microstructures and the performance of perovskite-based solar cells. Defects are also an important factor that influences the performance of the device. For example, point defects or intragrain interfaces can affect electron transport. Atomic-scale STEM facilitates a deeper understanding of the microstructure-property-performance relationship. For instance, using the RAT method proposed in this paper, the atom-scale intragrain strain distribution of OIHPs can be obtained by high-resolution STEM imaging (see Section 2.3), which offers an effective way to investigate the prominent strain effects on the performance of perovskite devices.

3. Conclusion

This study demonstrates that OIHPs can be released and transferred with high film integrity using a solution-phase method, unlocking atomic-scale investigation of perovskite lattice based on an STEM-DFT experiment-theory coupled approach. Strain relaxation is revealed with the RAT process of the film, endowing OIHPs with new (opto)electronic properties that are potentially different from those in regular OIHPs. Also importantly, this method can be applied to construct planar 2D–3D perovskite semiconductor heterojunctions. By leveraging the generality of this method, a range of intriguing single-layer perovskites, and dual-/multilayer perovskite heterojunctions may be fabricated, establishing a new platform for exploring novel semiconductor phenomena and functions.

4. Experimental Section

Raw Chemicals: $PbBr_2$ (≥99%), 4-tert-butylpyridine (TBP, 96%), Bis(trifluoromethane) sulfonimide lithium salt (99.95%), polystyrene (PS), and solvents such as dimethylformamide (DMF, 99.8%), dimethylsulfoxide (DMSO, 99.9%), chlorobenzene (CBE, 99.8%), acetonitrile (CH_3CN, >99.9%), and ethyl acetate (EA, 99.8%) were procured from Merck (USA). The chemicals $NH_2CH{=}NH_2Br$ (FABr, >99.99%), $NH_2CH{=}NH_2I$ (FAI, >99.99%), CH_3NH_3Cl (MACl, >99.99%), $C_8H_{12}IN$ (PEAI, >99.99%), and CH_3NH_3I (MAI, >99.99%) were purchased from Greatcell Solar (Australia). Tin (IV) oxide (15 wt% in H_2O colloidal dispersion) and CsI (99.998%) were acquired from Alfa Aesar (USA). Spiro-OMeTAD (99.8%) was procured from Borun Chemical Co., Ltd. (China). All chemicals were utilized without further purification.

MHP Precursor Solution, Film Synthesis, and RAT Processes: In this work, $FA_{0.8}Cs_{0.2}PbI_3$ and $FA_{0.9}Cs_{0.07}MA_{0.03}Pb(I_{0.92}Br_{0.08})_3$ perovskite films were utilized. For the preparation of $FA_{0.8}Cs_{0.2}PbI_3$ perovskite thin films, a perovskite precursor solution with a 1 M molar concentration was first created by dissolving 137.6 mg FAI, 52.0 mg CsI, and 461.0 mg PbI_2 in 1 mL of a mixed solvent of DMF/DMSO (v/v, 7:3). Subsequently, 50 µL of this precursor was spread onto PS-coated ITO substrates and subjected to a 3-stage spin-coating process (500 rpm for 5 s, 1000 rpm for 10 s, and 6000 rpm for 30 s). During the third stage, 400 µL of CBE was applied to the center of the spinning substrate. The spun films were then annealed at 90 °C for 30 min to form the final perovskite films. The transfer process of perovskites from the growth PS/glass substrates to new substrates was performed in a glove box. First, the growth substrates were dipped into CBE to dissolve the sacrificial layer PS and facilitate the detachment of the samples from the growth substrates. Next, vortex mixing or ultrasonication was employed to further detach the samples from the glass substrates. The resulting perovskite film was then separated from the substrate (as shown in Figure 1c). A new substrate with SnO_2 ETL was inserted between the perovskite film and the old substrate, and all the CBE was removed to allow the film to be adsorbed onto the new substrate. The transferred perovskite film was rinsed with clean CBE several times to remove any residual PS. The sample preparation for STEM followed the same method as the sample transfer method described previously. Additionally, TEM grids (Lacey/carbon grids on 200-mesh Cu, Ted Pella) were coated with one layer of C_{60} film to mitigate electron-beam damage. For comparison with the transferred sample, perovskite films directly fabricated on ITO substrates were prepared for XRD testing and focused ion beam (FIB) processing.

For the device demonstration, $FA_{0.9}Cs_{0.07}MA_{0.03}Pb(I_{0.92}Br_{0.08})_3$ perovskite films were utilized. To prepare these films, a perovskite precursor solution with a 1.35 M molar concentration was first created by dissolving 6.4 mg MAI, 13.5 mg FABr, 24.6 mg CsI, 39.6 mg $PbBr_2$, 190.4 mg FAI, and 574 mg PbI_2 in 1 mL of a mixed solvent of DMF/DMSO (v/v, 1:4). Next, 50 µL of this precursor was spread onto PS-coated ITO substrates and subjected to a 2-stage spin-coating process (1000 rpm for 10 s and then 4000 rpm for 30 s). During the second stage, 300 µL of EA was applied to the center of the spinning substrate. The spun films were then annealed at 90 °C for 30 min to form the final perovskite films. The transfer processes of $FA_{0.9}Cs_{0.07}MA_{0.03}Pb(I_{0.92}Br_{0.08})_3$ perovskite films followed the same method described above.

To prepare 2D perovskite ($(PEA)_2MAPb_2I_7$) thin films, a perovskite precursor solution with a 1 M molar concentration was first created by dissolving 249.0 mg PEAI, 79.5 mg MAI, and 461.0 mg PbI_2 in 1 mL of a mixed solvent of DMF/DMSO (v/v, 4:1). Next, 50 µL of this precursor was spread onto PS-coated ITO substrates, and the 2D films were then annealed at 90 °C for 30 min to form the final perovskite films. The transfer processes of $(PEA)_2MAPb_2I_7$ 2D perovskite thin films followed the same method as described above. The only difference is that the 2D perovskite film was transferred onto the surface of the 3D perovskite, which was also transferred to the substrate, as mentioned above. This means that the 2D and 3D perovskite films were transferred to the same substrate. It is also possible to prepare 2D perovskite films on 3D perovskite film surfaces and then transfer them together to a new substrate.

Materials Characterization and Property Measurement: X-ray diffraction (XRD) was conducted in the θ–2θ scan mode using a high-resolution diffractometer (D8 Advance, Bruker, USA) with Cu Kα_1 radiation (λ = 1.5406 Å). The limit of detection (LOD) for XRD is ≈1 wt%. Steady-state photoluminescence (PL) measurements were performed using a 375 nm picosecond laser (LDH-D-C-375, PicoQuant, Germany) as the excitation source. The PL signal was directed into a spectrograph (Ando Kymera 328i) and further collected by an electron multiplying charge-coupled

© 2023 The Authors. Advanced Optical Materials published by Wiley-VCH GmbH

21951071, 2024, 8, Downloaded from https://onlinelibrary.wiley.com/doi/10.1002/adom.202301255 by Hong Kong Poly University, Wiley Online Library on [17/06/2024]. See the Terms and Conditions (https://onlinelibrary.wiley.com/terms-and-conditions) on Wiley Online Library for rules of use; OA articles are governed by the applicable Creative Commons License

21951071, 2024, 8, Downloaded from https://onlinelibrary.wiley.com/doi/10.1002/adom.202301255 by Hong Kong Poly University, Wiley Online Library on [17/06/2024]. See the Terms and Conditions (https://onlinelibrary.wiley.com/terms-and-conditions) on Wiley Online Library for rules of use; OA articles are governed by the applicable Creative Commons License

device (EMCCD; Andor iXon Life 888, Oxford Instruments, UK) for steady-state PL analysis.

The cross-sectional TEM specimens of the thin films were prepared using a dual-beam FIB nanofabrication platform (Helios 5CX, Thermofisher, USA). STEM observations of the device cross-section specimens and transferred specimens were carried out using an aberration-corrected STEM microscope (Spectra-300, Thermofisher, USA; equipped with a field emission gun) with a 300 kV electron beam accelerating voltage. The probe convergence angle is 24.5 mrad, the HAADF detector's angular range is from 57 to 200 mrad, and the angular range of iDPC detector is 8–54 mrad. The dwell time of each pixel for the HAADF-STEM image and iDPC image acquisition is 6 and 5 µs, respectively. The size of all HAADF-STEM images is 2048×2048 pixel^2. The frame size is 18×18 nm^2 for the high-resolution HAADF-STEM images typical of those illustriously presented in this work. The average dose is from 1.62×10^4 e Å^2 for the acquisition of a single HAADF-STEM image.

To investigate the intragrain strain conditions in pristine and as-transferred OIHPs, geometric phase analysis (GPA) strain mapping was employed to extract the strain distribution from high-resolution HAADF-STEM images. The GPA software was developed as a plug-in for Gatan's DigitalMicrograph commercial software to measure lattice distortions in high-resolution transmission electron microscopy (HRTEM) images.[46,47]

DFT Calculations: DFT calculations were performed with the projector augmented wave (PAW) pseudopotentials and the Perdew–Burke–Ernzerhof (PBE) functional as implemented in the VASP package.[48,49] The plane wave cutoff energy was set to 450 eV, and the Γ-centered K-meshes with the *k*-spacing of 0.3 Å^{-1} were employed to sample the Brillouin zone. To simplify the calculations of $FA_{0.8}Cs_{0.2}PbI_3$ compounds, the A-site cations were all replaced by the FA, due to the little contribution of A-site cations to the band edges. The triaxial compression or tension was applied to the $FAPbI_3$ configuration to investigate the influence of strain release on the corresponding bandgap. For the electronic structure calculation, the spin–orbital coupling (SOC) effect was considered, and all models were fully relaxed until the energy difference was less than 10^{-4} eV and residual forces on each atom was smaller than 0.01 eV Å^{-1}.

Solar Cell Fabrication and Testing: The ITO glass substrates were sequentially washed with cleaning fluid, deionized water, ethanol, and isopropanol. The electron transport layer (ETL) was spin-coated onto the ITO glass substrate at 3000 rpm for 30 s, followed by annealing at 180 °C for 40 min in ambient air. The ETL-coated substrate was then transferred to a nitrogen-filled glovebox ($H_2O < 0.01$ ppm, $O_2 < 0.01$ ppm). The perovskite layer was transferred using the method described above. Subsequently, the Spiro-HTL was deposited on top of the perovskite layer by spin-coating at 4000 rpm for 30 s. Finally, a layer of 80 nm Au electrode was thermally evaporated onto the HTL to complete the devices. The current density–voltage (*J–V*) characteristics for PSCs were measured using a source meter (2612, Keithley, USA) under AM 1.5G one-sun illumination (100 mWcm^{-2}) generated by a solar simulator (Sirius-SS, Zolix, China) in the nitrogen-filled glovebox. The device area was defined with a shadow mask and was 0.05 cm^2. The scans were performed in the reverse direction (from V_{OC} to J_{SC}) over the voltage range of 0–1.3 V with a step size of 0.02 V and a dwell time of 10 ms. The light intensity was calibrated using a NREL-certified Si reference cell (Newport, USA). Steady-state current and PCE outputs were measured using a 2612 Source Meter (Keithley, USA) at the voltages determined from the maximum power points of the reverse-scan *J–V* curves.

Supporting Information

Supporting Information is available from the Wiley Online Library or from the author.

Acknowledgements

S.G. and X.Z. contributed equally to this work. S.C., S.G., W.W., and Z.L. acknowledged the support of startup grants from the Department of Applied Physics, the Hong Kong Polytechnic University (1-BD96, 1-BDCM), the Hong Kong Research Grants Council (RGC) General Research Fund (Nos. 15306021 and 15306122), and the open subject of National Laboratory of Solid State Microstructures, Nanjing University (No. M34001). Y.Z., X.Z., M.H., and T.D. acknowledged the Early Career Scheme (No. 22300221), General Research Fund (No. 12302822) from the Hong Kong RGC, and the Excellent Young Scientists Funds (No. 52222318) from National Natural Science Foundation of China. Y.Z. also acknowledged the start-up grant of HKUST. T.D. acknowledged the support of the RGC Postdoctoral Fellowship Scheme. X.Z. acknowledged the support of the K. C. Wong Education Foundation. The experimental assistance of T. Liu from ΣLab (www.alvinyzhou.com) is acknowledged.

Conflict of Interest

The authors declare no conflict of interest.

Data Availability Statement

Research data are not shared.

Keywords

halide perovskites, microstructure, scanning transmission electron microscopy, solar cells, transfer

Received: May 31, 2023
Revised: September 14, 2023
Published online: October 10, 2023

[1] W. Yang, B. Park, E. Jung, N. Jeon, Y. Kim, D. Lee, S. Shin, J. Seo, E. Kim, J. Noh, S. Seok, *Science* **2017**, *356*, 1376.
[2] E. Jung, N. Jeon, E. Park, C. Moon, T. Shin, T. Yang, J. Noh, J. Seo, *Nature* **2019**, *567*, 511.
[3] N. Jeon, H. Na, E. Jung, T. Yang, Y. Lee, G. Kim, H. Shin, S. Seok, J. Lee, J. Seo, *Nat. Energy* **2018**, *3*, 682.
[4] C. Stoumpos, C. Malliakas, M. Kanatzidis, *Inorg. Chem.* **2013**, *52*, 9019.
[5] M. Kumar, S. Dharani, W. Leong, P. Boix, R. Prabhakar, T. Baikie, C. Shi, H. Ding, R. Ramesh, M. Asta, M. Graetzel, S. Mhaisalkar, N. Mathews, *Adv. Mater.* **2014**, *26*, 7122.
[6] S. Pang, H. Hu, J. Zhang, S. Lv, Y. Yu, F. Wei, T. Qin, H. Xu, Z. Liu, G. Cui, *Chem. Mater.* **2014**, *26*, 1485.
[7] H. Min, D. Lee, J. Kim, G. Kim, K. Lee, J. Kim, S. Seok, *Nature* **2021**, *598*, 444.
[8] J. Jang, Y. Park, E. Cha, S. Ji, H. Hwang, G. Kim, J. Jin, J. Park, *Adv. Mater.* **2021**, *33*, 2101093.
[9] J. A. Pan, J. Ondry, D. Talapin, *Nano Lett.* **2021**, *21*, 7609.
[10] Y. Zou, L. Cai, T. Song, B. Sun, *Small Sci.* **2021**, *1*, 2000050.
[11] D. Ji, S. Cai, T. Paudel, H. Sun, C. Zhang, L. Han, Y. Wei, Y. Zang, M. Gu, Y. Zhang, W. Gao, H. Huyan, W. Guo, D. Wu, Z. Gu, E. Tsymbal, P. Wang, Y. Nie, X. Pan, *Nature* **2019**, *570*, 87.
[12] Y. Zhou, H. Sternlicht, N. P. Padture, *Joule* **2019**, *3*, 641.
[13] M. U. Rothmann, W. Li, Y. Zhu, U. Bach, L. Spiccia, J. Etheridge, Y. Cheng, *Nat. Commun.* **2017**, *8*, 14547.
[14] M. U. Rothmann, J. S. Kim, J. Borchert, K. B. Lohmann, C. M. O'Leary, A. A. Sheader, L. Clark, H. J. Snaith, M. B. Johnston, P. D. Nellist, L. M. Herz, *Science* **2020**, *370*, eabb5940.
[15] Y. Zhou, L. M. Herz, A. K. Jen, M. Saliba, *Nat. Energy* **2022**, *7*, 794.
[16] R. Chen, Y. Wu, Y. Wang, R. Xu, R. He, Y. Fan, X. Huang, J. Yin, B. Wu, J. Li, N. Zheng, *Adv. Funct. Mater.* **2021**, *31*, 2008760.

© 2023 The Authors. Advanced Optical Materials published by Wiley-VCH GmbH

[17] S. Ganesan, M. V. Rajendran, R. K. Raman, V. S. Menon, A. Krishnamoorthy, *Int. J. Energy Res.* **2022**, *46*, 15571.
[18] H. Zhou, L. Yang, Y. Duan, M. Wu, Y. Li, D. Xu, H. Zou, J. Wang, S. Yang, Z. Liu, *Adv. Energy Mater.* **2023**, *13*, 220437.
[19] A. Guerrero, G. Garcia-Belmonte, I. Mora-Sero, J. Bisquert, Y. Kang, T. J. Jacobsson, J. Correa-Baena, A. Hagfeldt, *J. Phys. Chem. C* **2016**, *120*, 8023.
[20] H. P. Wang, S. Li, X. Liu, Z. Shi, X. Fang, J. H. He, *Adv. Mater.* **2021**, *33*, 2003309.
[21] F. Cao, Z. Li, X. Liu, Z. Shi, X. Fang, *Adv. Funct. Mater.* **2022**, *32*, 2206151.
[22] J. W. Lee, S. G. Kim, S. H. Bae, D. K. Lee, O. Lin, Y. Yang, N. G. Park, *Nano Lett.* **2017**, *17*, 4270.
[23] A. Ng, Z. Ren, Q. Shen, S. H. Cheung, H. C. Gokkaya, G. Bai, J. Wang, L. Yang, S. K. So, A. B. Djuriši, W. W. Leung, J. Hao, W. K. Chan, C. Surya, *J. Mater. Chem. A* **2015**, *3*, 9223.
[24] Z. Ren, A. Ng, Q. Shen, H. C. Gokkaya, J. Wang, L. Yang, W.-K. Yiu, G. Bai, A. B. Djuriši, W. W. Leung, J. Hao, W. K. Chan, *Sci. Rep.* **2014**, *4*, 6752.
[25] J. Burschka, N. Pellet, S.-J. Moon, R. Humphry-Baker, P. Gao, M. K. Nazeeruddin, M. Grätzel, *Nature* **2013**, *499*, 316.
[26] Y. H. Lee, J. Luo, R. Humphry-Baker, P. Gao, M. Grätzel, M. K. Nazeeruddin, *Adv. Funct. Mater.* **2015**, *25*, 3925.
[27] L. L. Wang, C. McCleese, A. Kovalsky, Y. X. Zhao, C. Burda, *J. Am. Chem. Soc.* **2014**, *136*, 12205.
[28] M. Hao, T. Duan, Z. Ma, M. Ju, J. A. Bennett, T. Liu, P. Guo, Y. Zhou, *Adv. Mater.* **2023**, *35*, 2211155.
[29] B. Shen, X. Chen, X. Fan, H. Xiong, H. Wang, W. Qian, Y. Wang, F. Wei, *Nat. Commun.* **2021**, *12*, 2212.
[30] H. Xiong, Z. Liu, X. Chen, H. Wang, W. Qian, C. Zhang, A. Zheng, F. Wei, *Science* **2022**, *376*, 491.
[31] H. Wang, L. Liu, J. Wang, C. Li, J. Hou, K. Zheng, *Molecules* **2022**, *27*, 3829.
[32] S. Cai, J. Dai, Z. Shao, M. U. Rothmann, Y. Jia, C. Gao, M. Hao, S. Pang, P. Wang, S. Lau, K. Zhu, J. J. Berry, L. M. Herz, X. Zeng, Y. Zhou, *J. Am. Chem. Soc.* **2022**, *144*, 1910.
[33] S. Y. Leblebici, L. Leppert, Y. Li, S. E. Reyes-Lillo, S. Wickenburg, E. Wong, J. Lee, M. Melli, D. Ziegler, D. K. Angell, D. F. Ogletree, P. D. Ashby, F. M. Toma, J. B. Neaton, I. D. Sharp, A. Weber-Bargioni, *Nat. Energy* **2016**, *1*, 16093.
[34] H. Kim, N. Park, *NPG Asia Mater.* **2020**, *12*, 78.
[35] T. W. Jones, A. Osherov, M. Alsari, M. Sponseller, B. C. Duck, Y. Jung, C. Settens, F. Niroui, R. Brenes, C. V. Stan, Y. Li, M. Abdi-Jalebi, N. Tamura, J. E. Macdonald, M. Burghammer, R. H. Friend, V. Bulović, A. Walsh, G. J. Wilson, S. Lilliu, S. D. Stranks, *Energy Environ. Sci.* **2019**, *12*, 596.
[36] J. Wu, S. Liu, Z. Li, S. Wang, D. Xue, Y. Lin, J. Hu, *Natl. Sci. Rev.* **2021**, *8*, nwab047.
[37] T. J. Jacobsson, L. J. Schwan, M. Ottosson, A. Hagfeldt, T. Edvinsson, *Inorg. Chem.* **2015**, *54*, 10678.
[38] V. Craciun, D. Craciun, X. Wang, T. J. Anderson, R. K. Singh, *Adv. Mater.* **2003**, *5*, 401.
[39] D. Liu, D. Luo, A. N. Iqbal, K. W. P. Orr, T. A. S. Doherty, Z. Lu, S. D. Stranks, W. Zhang, *Nat. Mater.* **2021**, *20*, 1337.
[40] C. Zhu, X. Niu, Y. Fu, N. Li, C. Hu, Y. Chen, X. He, G. Na, P. Liu, H. Zai, Y. Ge, Y. Lu, X. Ke, Y. Bai, S. Yang, P. Chen, Y. Li, M. Sui, L. Zhang, H. Zhou, Q. Chen, *Nat. Commun.* **2019**, *10*, 815.
[41] D. J. Xue, Y. Hou, S. C. Liu, M. Wei, B. Chen, Z. Huang, Z. Li, B. Sun, A. H. Proppe, Y. Dong, M. I. Saidaminov, S. O. Kelley, J. S. Hu, E. H. Sargent, *Nat. Commun.* **2020**, *11*, 1514.
[42] B. Murali, E. Yengel, W. Peng, Z. Chen, M. S. Alias, E. Alarousu, B. S. Ooi, V. Burlakov, A. Goriely, M. Eddaoudi, O. M. Bakr, O. F. Mohammed, *J. Phys. Chem. Lett.* **2017**, *8*, 137.
[43] J. Zhao, Y. Deng, H. Wei, X. Zheng, Z. Yu, Y. Shao, J. E. Shield, J. Huang, *Sci. Adv.* **2017**, *3*, eaao5616.
[44] W. Li, M. U. Rothmann, Y. Zhu, W. Chen, C. Yang, Y. Yuan, Y. Y. Choo, X. Wen, Y. Cheng, U. Bach, J. Ethe, *Nat. Energy* **2021**, *6*, 624.
[45] T. Duan, W. Wang, S. Cai, Y. Zhou, *ACS Energy Lett.* **2023**, *8*, 3048.
[46] M. J. Hÿtch, E. Snoeck, R. Kilaas, *Ultramicroscopy* **1998**, *74*, 131.
[47] M. Takeda, J. Suzuki, *J. Opt. Soc. Am. A* **1996**, *13*, 1495.
[48] G. Kresse, J. Furthmuller, *Phys. Rev. B* **1996**, *54*, 11169.
[49] J. P. Perdew, K. Burke, M. Ernzerhof, *Phys. Rev. Lett.* **1996**, *77*, 3865.

© 2023 The Authors. Advanced Optical Materials published by Wiley-VCH GmbH

21951071, 2024, 8, Downloaded from https://onlinelibrary.wiley.com/doi/10.1002/adom.202301255 by Hong Kong Poly University, Wiley Online Library on [17/06/2024]. See the Terms and Conditions (https://onlinelibrary.wiley.com/terms-and-conditions) on Wiley Online Library for rules of use; OA articles are governed by the applicable Creative Commons License